Mechanism of the Reaction of CH_3SO with NO_2 in Relation to Atmospheric Oxidation of Dimethyl Sulfide: Experimental and Theoretical Study

Alexander Kukui,* Valérie Bossoutrot, Gérard Laverdet, and Georges Le Bras

Laboratoire de Combustion et Systèmes Réactifs, C.N.R.S., 1c av. de la Recherche Scientifique,
45071 Orléans Cedex 2, France

Received: September 7, 1999; In Final Form: November 17, 1999

CH_3SO_2 radical decomposition and the mechanism of SO_2 and CH_3 formation in the reaction of CH_3SO with NO_2 were experimentally investigated in the pressure range 1−612 Torr of He using laser pulsed photolysis/laser-induced fluorescence and discharge flow mass spectrometry/laser-induced fluorescence techniques. The upper limit for the thermal decomposition rate of CH_3SO_2 in the investigated pressure range has been found to be 100 s^{-1} at 300 K. High-pressure limit, $k^{\infty} = 2.08 \times 10^3$ s^{-1}, and low-pressure limit, $k^0 = 2.72 \times 10^{-17}$ cm^3 $molecule^{-1}$ s^{-1}, of the rate coefficient of the CH_3SO_2 decomposition have been derived from ab initio and RRKM calculations. The CH_3SO_2 decomposition rate at 760 Torr and 300 K has been estimated to be about 200 s^{-1} from falloff calculations. Reaction of CH_3SO with NO_2 has been found to form CH_3 and SO_2 with a yield varying from (0.33 ± 0.05) at 13 Torr to (0.18 ± 0.03) at 612 Torr of He. The rate constant for the reaction of CH_3SO with NO_2 has been found to be $(1.5 \pm 0.4) \times 10^{-11}$ cm^3 $molecule^{-1}$ s^{-1} at 300 K, independent of pressure. On the basis of ab initio and RRKM calculations, the experimental results have been interpreted by assuming the reaction of CH_3SO with NO_2 to form chemically activated CH_3SO_2* radical followed by its thermal stabilization or prompt decomposition to CH_3 and SO_2. The implication of the obtained results for the atmospheric oxidation of dimethyl sulfide is discussed.

Introduction

Release of dimethyl sulfide (DMS) by marine biota has been recognized as the largest natural global source of sulfur in the atmosphere exceeding anthropogenic sulfur emissions in the southern hemisphere.[1] Atmospheric oxidation of DMS has been suggested to play an important role in the formation of clouds by producing new sulfate particles which act as cloud condensation nuclei (CCN).[2] This source of non-sea-salt sulfate is considered to be predominantly the gas-phase oxidation of SO_2 to H_2SO_4 by reaction with the OH radical. Knowledge of the SO_2 yield from DMS oxidation is therefore crucial to assess the capacity of DMS to produce aerosol. The SO_2 yield is determined by the mechanism of DMS oxidation which is quite complex and far from being well understood. It is now known that the main initiation step of DMS oxidation is the reaction with OH which proceeds by both abstraction and addition channels, the latter being dominant at low temperatures.[3] The other significant channel, the reaction with NO_3, appears to proceed exclusively by hydrogen abstraction.[4] Based mostly on field measurements and chamber type studies,[5,6] the main oxidation products are believed to be, besides SO_2, methane sulfonic acid (MSA) and dimethyl sulfone ($DMSO_2$), although the mechanism of their formation remains poorly defined in terms of elementary reactions.[7] The relative yields of the products may also strongly depend on temperature and other atmospheric conditions, like NO_x concentration or intensity of vertical mixing. In fact, no reliable and unambiguous data exist on the correlation between products yields and atmospheric parameters. Considering the complexity of the system, experimental studies of the elementary steps involved in DMS oxidation remain of prime importance.

One of the possible key intermediates in DMS oxidation mechanism is the methylsulfonyl radical (CH_3SO_2).[8] It may be formed either directly in reactions of the CH_3SO intermediate with NO_2 and O_3 or via isomerization of CH_3SOO generated by addition of O_2 to CH_3S.[9] The CH_3SO radical is produced in the abstraction route of the OH oxidation mechanism and in the NO_3 oxidation through the sequence involving the $CH_3SCH_2O_2$ and CH_3S intermediates. CH_3SO has also been suggested to be formed in the OH addition reaction through dimethyl sulfoxide (DMSO) in a mechanism involving H atom abstraction from DMSO by OH.[6] However, it has recently been shown in a more direct study that the OH reaction with DMSO produces methane sulfinic acid (MSIA), $CH_3S(O)OH$, which may react with OH to produce CH_3SO_2.[10] Then, both mechanisms suggested for the OH addition reaction of DMS would produce CH_3SO_2. This radical would be, therefore, an intermediate in all the oxidation routes of DMS. In such a case, the reactions of CH_3SO_2 formation and fate may influence the SO_2 and MSA yield and hence the capacity of DMS to produce new CN from SO_2 oxidation. CH_3SO_2 can decompose to CH_3 and SO_2 or react with O_2, O_3, and NO_2 to produce CH_3SO_3 and possibly MSA.

The stability of the CH_3SO_2 radical and its reaction with NO_2 have been investigated recently in this laboratory by Ray et al.[11] using the discharge flow LIF/MS method. The decomposition of CH_3SO_2 has been found to be very fast, with a rate around 500 s^{-1} at 0.75 Torr of He and at room temperature. In the present work, decomposition of CH_3SO_2 radical and the mechanism of the reaction of CH_3SO with NO_2 were further investigated in an extended pressure range by monitoring the absolute yields and kinetics of SO_2 and CH_3O. Theoretical analysis of experimental data is also presented.

---

* Corresponding author. E-mail: kukuy@cnrs-orleans.fr.

10.1021/jp993158i CCC: $19.00

Experimental Section

Two different experimental setups have been employed in this study. The experiments at low pressure, 1 Torr of He, were conducted in a discharge fast flow reactor coupled to a combined mass spectrometric/laser-induced fluorescence detection system (DF-MS/LIF). For the experiments at 30−600 Torr of He, a pulsed laser photolysis with LIF detection (PLP-LIF) technique has been used.

Pulsed Laser Photolysis/LIF Experimental Setup. The PLP-LIF experiments were performed by photolyzing CH_3SSCH_3 (DMDS) or CH_3I in DMDS/NO_2/He or CH_3I/NO_2/He mixtures, respectively, and by monitoring the CH_3O radical kinetics by LIF. The CH_3O profiles obtained by photolysis of CH_3I/NO_2/He mixtures were used for CH_3O calibration and for the determination of the rate constants for the reactions of CH_3 and CH_3O with NO_2, as described in the Results section.

The reaction cell was similar to that previously described by Mellouki et al.[12] It consisted of a jacketed 4.5 cm diameter Pyrex flow tube with 15 cm long orthogonal sidearms equipped with light baffles and quartz windows. The temperature in the reactor was maintained with an accuracy of ±1 K by flowing temperature regulated liquid through the jacket. The photolysis and probe beams were perpendicular to each other and to the flow direction. The delay time between the photolysis and probe lasers was varied from 10 μs to 1 ms.

The photolysis was performed at 248 or 351 nm using a KrF or XeF Lambda Physik excimer laser operating at a 5−10 Hz pulse repetition rate. The pulse energy of the ~1 cm diameter excitation laser beam was kept below 1 mJ cm^{-2} using a neutral-density filter.

CH_3O was detected by pumping of its $A^2A_1 \leftarrow X^2E$ transition at 292.8 nm using frequency doubled output of a Lambda Physik FL3002 tunable dye laser (Rhodamine 6G dye) pumped by a Continuum Surelite I-10 Nd:YAG laser. The dye laser pulse energy was ca. 0.1 mJ and was monitored after passing the fluorescence cell by a LAS PM200 pyroelectric detector for every pulse.

The fluorescence light was detected by a Hamamatsu R2560 photomultiplier after passing through a band-pass filter. The multiplier output was amplified with a fast preamplifier SRS D-300. The LIF signal was registered in a photon-counting integration mode using a SR430 multichannel scaler/averager. The gate of the counter was opened with a delay of 0.1 μs after the laser pulse. The gate width was 2−5 μs. The fluorescence signal was normalized to the average probe pulse energy upon integration of 100−200 laser shots.

DMDS (or CH_3I) and NO_2 diluted in He were added to the He carrier gas flow in the glass manifold. No difference has been found when the reactants were injected directly into the flow cell, suggesting a negligible influence of possible heterogeneous reactions of DMDS and NO_2. Flow velocities were in the range (5−100) cm s^{-1}, while the laser pulse repetition rates were chosen to ensure mixture renewal between two pulses. Typical concentrations of DMDS, CH_3I, and of NO_2 used in the present experiments are presented in the comments to Table 2. Further experimental details are presented in the Experimental Results section.

Discharge Flow−MS/LIF Experimental Setup. The experimental setup was similar to that used in the previous investigation of the CH_3SO_2 decomposition[11] with some modifications for the detection of CH_3O and SO_2. The reactor consisted of a 36 mm i.d., 400 mm long quartz flow tube and a movable inlet tube of 15 mm i.d. made of Pyrex. Both tubes had sidearms, each equipped with inlet ports and microwave cavities for F or Cl atoms generation. For the source of F atoms, ceramic (Al_2O_3) inserts were used in the discharge region. Inner surfaces of the reactor were coated with Halocarbon wax. Inner surfaces of the injector were coated with phosphoric acid to minimize wall loss of Cl atoms. Flow velocities of He were in the range 5−19 m s^{-1} at a total pressure of 1 Torr of He.

CH_3S was produced via the fast reaction $CH_3SH + Cl \rightarrow CH_3S + HCl$ ($k = 2 \times 10^{-10}$ cm^3 $molecule^{-1}$ s^{-1}),[13] with subsequent conversion of CH_3S to CH_3O and SO_2 as described in the next section. All experiments were performed in excess concentrations of NO_2 and CH_3SH over Cl atoms. Typical concentrations of NO_2, CH_3SH, and Cl were $(0.5-50) \times 10^{14}$, $(3-10) \times 10^{13}$, and $(5-20) \times 10^{10}$ molecules cm^{-3}, respectively. NO_2 and CH_3SH were introduced directly into the main flow tube via a sidearm. Chlorine atoms were produced by passing Cl_2/He mixtures through a microwave discharge and added to the mixture of NO_2 and CH_3SH via the movable injector.

The LIF signal recorded from the Cl/CH_3SH/NO_2 reaction mixture resulted from the fluorescence of both CH_3O and SO_2. The kinetic measurements were performed by monitoring LIF signals at several, four or six, excitation wavelengths in the range 289−295 nm as a function of reaction time. Extraction of CH_3O and SO_2 specific contributions from the LIF composite signal was performed by a least-squares method using known relative signal intensities at the used wavelengths for CH_3O and SO_2 measured routinely for every experimental run. LIF signal excitation and detection schemes were the same as described for laser photolysis experiments with the difference that the dye laser was pumped by a Lambda Physik excimer (XeCl) laser operated at a pulse repetition rate of 20 Hz.

Reference methoxy radical LIF excitation spectra were recorded using reaction of CH_3 with NO_2 as the source of CH_3O. CH_3 radicals were produced by reaction of F atoms with methane. LIF spectra of SO_2 and absolute sensitivity of the LIF detection system to SO_2 were obtained by adding a known concentration of SO_2 to the investigated reaction mixture without discharge and by recording the resulting spectra.

Chlorine atom concentrations were determined by mass spectrometric measurements of the yield of vinyl chloride, C_2H_3Cl, in the titration reaction of Cl with vinyl bromide, C_2H_3Br.[14]

Experimental Results

Pulsed Laser Photolysis/LIF Results. In the experiments using photolysis of DMDS/NO_2 mixtures either at 248 nm or at 351 nm the CH_3O radical has been detected with typical dependence of LIF signal intensity on reaction time as shown in Figure 1. The mechanism used for the treatment of the CH_3O kinetics includes reactions 1−9, and it is described below.

The photolysis of DMDS at 248 nm may proceed via several thermochemically feasible channels, but the most likely channel is that forming two CH_3S radicals:

$$CH_3SSCH_3 + h\nu\ (248\ \text{nm}) \rightarrow 2\ CH_3S \qquad (1a)$$

Barone et al.[15] have determined a yield of CH_3S of (1.65 ± 0.38), with a negligible production of H atoms. Lee et al.[16] have studied the photodissociation of DMDS by translational spectroscopy and concluded that dissociation occurs predominantly via S−S bond scission. On the basis of these results, we assumed that only channel 1a occurs corresponding to a photolysis yield of CH_3S from DMDS of two.

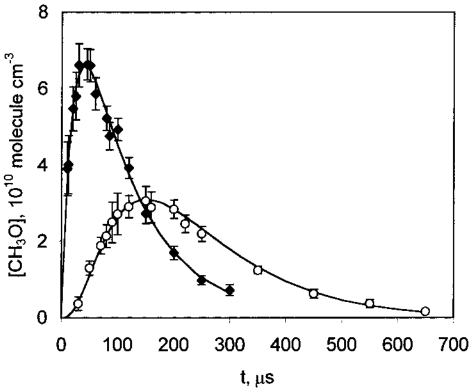

Figure 1. Time dependencies of CH_3O concentrations in the photolysis of CH_3I (◆) and DMDS (○) in the presence of NO_2 at $p = 100$ Torr, $T = 300$ K, and $[NO_2] = 8.58 \times 10^{14}$ molecules cm^{-3}. Solid lines represent concentration profiles calculated using reaction rate constants $k_5 = 5.77 \times 10^{-11}$, $k_9 = 1.17 \times 10^{-11}$, $k_4 = 1.09 \times 10^{-11}$, in units cm^3 $molecule^{-1}$ s^{-1}, and $\alpha_4 = k_{4b}/k_4 = 0.14$.

The CH_3S radical produced via reaction 1a reacts with NO_2 to form CH_3SO:

$$CH_3S + NO_2 \rightarrow CH_3SO + NO \qquad (2)$$

This fast reaction has been found to produce CH_3SO with a unity yield at 297 K and 1 Torr of He.[17] This is in agreement with a NO yield of (0.8 ± 0.2) measured by Tyndall and Ravishankara.[18] Taking into account the pressure independence of k_2 in the range 3−200 Torr and only a weak temperature dependence,[19,20] we assumed CH_3SO to be formed with a unity yield in reaction 2 for the pressure and temperature ranges of our experiments.

At 248 nm photolysis, an additional source of CH_3S and CH_3SO radicals is the reaction of DMDS with O atoms generated by photolysis of NO_2 ($k_3 = 1.5 \times 10^{-10}$ cm^3 $molecule^{-1}$ s^{-1}):[21]

$$O + CH_3SSCH_3 \rightarrow CH_3S + CH_3SO \qquad (3)$$

Initial concentrations of O atoms, $[O]_0 = (0.1-2) \times 10^{11}$ molecules cm^{-3} at $\lambda = 248$ nm, were calculated using known excimer laser fluence and NO_2 photolysis cross section. The resulting corrections for the initial concentrations of CH_3S and CH_3SO depended on the ratio of the initial DMDS and NO_2 concentrations and were in the range 1−30%, as determined from the numerical simulations and estimated from the ratio of initial concentrations of CH_3S and CH_3SO produced from reaction 3 to the initial CH_3S concentration generated by DMDS photolysis. The ratio is equal to $(\sigma_{NO_2}/\sigma_{DMDS})/(k_{O+NO_2}/k_3 + [DMDS]/[NO_2])$, σ_{NO_2} and σ_{DMDS} being the absorption cross sections of NO_2 and DMDS at 248 nm and k_{O+NO_2} the rate constant of $O + NO_2$ reaction ($k_{O+NO_2} = 9.7 \times 10^{-12}$ cm^3 $molecule^{-1}$ s^{-1}).[21]

Several experiments were performed by photolyzing DMDS/NO_2 mixtures at 351 nm. In this case, reaction 3 was the main source of CH_3S and CH_3SO radicals, photolysis of DMDS being negligible compared to that of NO_2.

The CH_3SO radical reacts predominantly with NO_2 ($k_4 = (1.2 \pm 0.25) \times 10^{-11}$ cm^3 $molecule^{-1}$ s^{-1} at 1 Torr of He):[17]

$$CH_3SO + NO_2 \rightarrow \text{products} \qquad (4)$$

The products of reaction 4 have not been directly identified, although indirect evidence of CH_3SO_2 formation has been found. Tyndall and Ravishankara[18] suggested CH_3SO_2 formation according to reaction 4a on the basis of kinetics and absolute yield of NO observed by photolyzing DMDS in the presence of NO_2:

$$CH_3SO + NO_2 \rightarrow CH_3SO_2 + NO \qquad (4a)$$

Ray et al.[11] assumed CH_3SO_2 formation and its fast decomposition to CH_3 and SO_2 from the CH_3O and SO_2 kinetics measured by LIF in discharge flow reactor experiments. Similarly to Ray et al.,[11] formation of the CH_3O radical, observed in the present work, has been assigned to the reaction sequence including formation of the CH_3 radical followed by its reaction with NO_2 (5a):

$$CH_3 + NO_2 \rightarrow CH_3O + NO \qquad (5a)$$

Direct formation of CH_3O in the reaction of CH_3SO with NO_2 is endothermic by about 33 kcal/mol and therefore negligible.

The source of CH_3 may be either the thermal unimolecular decomposition of CH_3SO_2 (6) or the reaction of CH_3SO with NO_2 (4b):

$$CH_3SO_2 + He \rightarrow CH_3 + SO_2 + He \qquad (6)$$

$$CH_3SO + NO_2 \rightarrow CH_3 + SO_2 + NO \qquad (4b)$$

As it is discussed below, formation of CH_3 and SO_2 may also proceed via a mechanism, including formation of a chemically activated CH_3SO_2* radical in reaction 4, and its prompt decomposition which would compete with its thermalization. Nevertheless, as the prompt decomposition/thermalization processes proceed on a time scale of 10^{-8}−10^{-7} s, the two different mechanisms are equivalent as to the description of CH_3O and SO_2 concentration profiles which, therefore, have been analyzed assuming a mechanism including reactions 4a and 4b.

In addition to reaction 6, another removal process of CH_3SO_2 may be its reaction with NO_2 (7), which may also lead to the formation of CH_3 via decomposition of CH_3SO_3 (8) formed in (7a):

$$CH_3SO_2 + NO_2 \rightarrow CH_3SO_3 + NO \qquad (7a)$$

$$\rightarrow CH_3 + SO_3 + NO \qquad (7b)$$

$$\rightarrow \text{products} \qquad (7c)$$

$$CH_3SO_3 + He \rightarrow CH_3 + SO_3 + He \qquad (8)$$

The CH_3O radical formed in reaction 5a is predominantly consumed in reaction with NO_2:

$$CH_3O + NO_2 \rightarrow \text{products} \qquad (9)$$

The experimental CH_3O concentration profiles were analyzed in order to determine the rate constants for reactions 4, 6, and 7. For this reaction system the influence of diffusion on the rate parameters derived from modeling may be significant. The influence becomes stronger at low pressures and low reaction rates, e.g., low NO_2 concentrations in our system. Characteristic diffusion time has been roughly estimated from the expression $t_D = R^2/4D$, where R is a radius of the detection zone and D the diffusion coefficient of the reactive species in He. At 10 and 100 Torr pressure $t_D \approx 5$ and 50 ms, respectively. The concentration of NO_2 used in the experiments, $[NO_2] > 10^{14}$ molecules cm^{-3}, was high enough to make the time constant for reaction at least 10 times shorter than the estimated characteristic time of diffusion.

TABLE 1: Reactions Used for Simulation of CH_3O Concentration Profiles

	reaction	k, cm^3 molecule^{-1} s^{-1}	ref
2	$CH_3S + NO_2 \rightarrow CH_3SO + NO$	6.1×10^{-11}	19
4b	$CH_3SO + NO_2 \rightarrow CH_3 + SO_2 + NO$	variable	
4a	$CH_3SO + NO_2 \rightarrow CH_3SO_2 + NO$	variable	
6	$CH_3SO_2 \rightarrow CH_3 + SO_2$	variable	
7a	$CH_3SO_2 + NO_2 \rightarrow CH_3SO_3 + NO$	variable	
8	$CH_3SO_3 \rightarrow CH_3 + SO_3$	variable	
5b	$CH_3 + NO_2 + He \rightarrow$ products	See text	
5a	$CH_3 + NO_2 \rightarrow CH_3O + NO$	2.5×10^{-11}	25
9a	$CH_3O + NO_2 + He \rightarrow CH_3ONO_2 + He$	See text	
9b	$CH_3O + NO_2 \rightarrow CH_2O + HONO$	2.0×10^{-13}	21
10a	$O + CH_3I \rightarrow CH_3 + IO$	0.79×10^{-11}	28
10b	$O + CH_3I \rightarrow CH_2I + OH$	0.29×10^{-11}	28
10c	$O + CH_3I \rightarrow$ products	0.72×10^{-11}	28
3	$O + CH_3SSCH_3 \rightarrow CH_3S + CH_3SO$	1.51×10^{-10}	21
11	$O + NO_2 \rightarrow O_2 + NO$	9.73×10^{-12}	21

Simulation of the experimental CH_3O profiles was performed using the rate constant $k_2 = 6.1 \times 10^{-11}$ cm^3 molecule^{-1} s^{-1}.[19] The rate constants used for the reactions of CH_3 and CH_3O with NO_2 were those determined in this work from the CH_3O concentration profiles obtained from photolysis of CH_3I/NO_2 mixtures (see next section).

The reaction of CH_3O with NO_2 has been studied previously in the pressure ranges 1−10 Torr [22] and 30−100 Torr of He.[23,24] The comparison of k_9 derived from our experiments with the previous results has been used as a test.

The reaction of CH_3 with NO_2 proceeds via two channels, reaction 5a and the pressure-dependent channel 5b:

$$CH_3 + NO_2 + He \rightarrow CH_3NO_2\ (CH_3ONO) + He \quad (5b)$$

Then, the pressure dependence of the CH_3O yield had to be considered. At low pressure, the fast reaction 5a forming CH_3O is predominant ($k_{5a} = 2.5 \times 10^{-11}$ cm^3 molecule^{-1} s^{-1} at 1 Torr of He).[25] The addition channel (5b) forming CH_3NO_2 or CH_3ONO is known,[26] but no direct measurement of the rate constant at room temperature and in the pressure range of our study has been reported so far.

In this work, the pressure dependence of the total rate constant k_5 and of the CH_3O yield has been accounted for by recording the CH_3O concentration profiles from CH_3I/NO_2 photolysis. These were recorded under the same experimental conditions (NO_2 concentration, pressure, flow conditions, and lasers fluence) as for the experimental runs with DMDS/NO_2 mixtures.

CH_3I/NO_2 Photolysis. Photolysis of CH_3I is known to produce the CH_3 radical with unity quantum yield.[27] In a large excess of NO_2, the dependence of the experimental CH_3O LIF signal intensity, I^{CH_3I}, on reaction time t is determined mainly by the reaction of CH_3O formation (5) and the consumption reaction with NO_2 (9).

For the determination of k_5 and k_9, the following procedure has been used. First, the rate constant k_9 was estimated from the quasilinear dependencies of ln $I^{CH_3I} = f(t)$ at long reaction times where reaction 5 became less significant compared to reaction 9. This estimation of k_9 was used in the optimization of k_5 by least-squares fitting of the CH_3O profiles. Finally, the two parameters, k_5 and k_9, were optimized simultaneously by least-squares fitting, using the estimated k_5 and k_9 as initial values for the optimization. The two-parameter optimization was performed using the set of reactions listed in Table 1. In addition to reactions 5 and 9, the reaction of O atoms with CH_3I (10) was of importance in the experiments with a low $[CH_3I]/[NO_2]$ ratio:

$$O + CH_3I \rightarrow IO + CH_3 \quad (10a)$$

Reaction 10 ($k_{10} = 1.7 \times 10^{-11}$ cm^3 molecule^{-1} s^{-1})[28] has been reported to proceed with a CH_3 yield of 44% ± 4% and a negligible yield of CH_3O.[28]

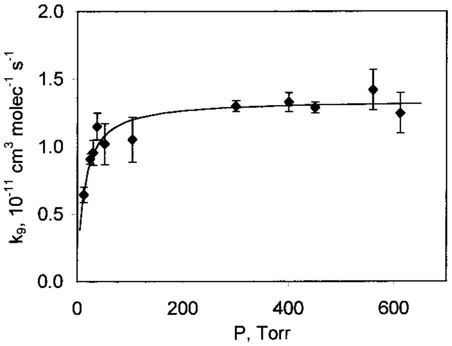

Figure 2. Pressure dependence of the second-order rate constant for the reaction of CH_3O with NO_2 (9): (◆) experimental points; (solid line) falloff curve calculated using parameters from Frost and Smith.[24]

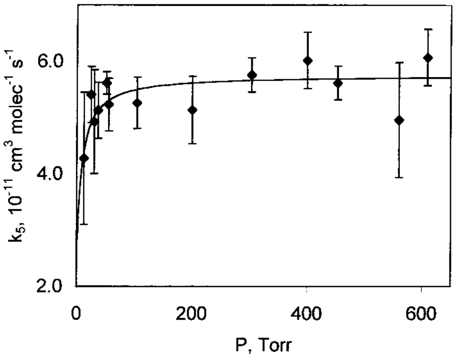

Figure 3. Pressure dependence of the second-order rate constant for the reaction of CH_3 with NO_2: (◆) experimental points; (solid line) calculated falloff curve (see text).

The results obtained in this work for the pressure dependence of k_9 and k_5 are presented in Figures 2 and 3, respectively. For reaction 9, the results are in good agreement with those of Frost and Smith.[24] The data for reaction 5b were fitted to the falloff curve described by the Troe expression,[29] while the rate constant for reaction 5a has been considered to be independent of pressure ($k_{5a} = 2.5 \times 10^{-11}$ cm^3 molecule^{-1} s^{-1}).[25] Using a broadening factor of 0.6, the following low-pressure and high-pressure limit values of k_{5b} have been derived at 300 K:

$$k^0_{5b} = (2 \pm 1) \times 10^{-28}\ \text{cm}^6\ \text{molecule}^{-2}\ \text{s}^{-1}$$

and

$$k^\infty_{5b} = (4.2 \pm 0.5) \times 10^{-11}\ \text{cm}^3\ \text{molecule}^{-1}\ \text{s}^{-1}$$

The only previous estimation $k^\infty_{5b} = 3.44 \times 10^{-11}$ cm^3 molecule^{-1} s^{-1} [26] is in fair agreement with our result. The present determination of k^0_{5b} can be compared with the low-pressure limit value $(6 \pm 2) \times 10^{-29}$ cm^6 molecule^{-2} s^{-1}, estimated for the CH_3NO_2 formation channel by McCaulley et al.[30] Considering the given uncertainty ranges and taking into account the possible contribution of the reaction channel forming CH_3ONO to the rate constant k^0_{5b} determined in this work, as well as a somewhat arbitrary value chosen for the broadening factor, these results may be considered as consistent.

TABLE 2: Experimental Results Obtained by Photolyzing DMDS/NO_2 and CH_3I/NO_2 Mixtures at 248 and 351 nm[a]

P, Torr	k_9, 10^{-11} cm^3 $molecule^{-1}$ s^{-1}	k_5, 10^{-11} cm^3 $molecule^{-1}$ s^{-1}	k_4, 10^{-11} cm^3 $molecule^{-1}$ s^{-1}	$\alpha_4 = k_{4b}/k_4$
$T = 300$ K				
12[b]	0.64 ± 0.06	4.28 ± 1.2	1.99 ± 0.3	0.33 ± 0.05
30[b]	0.96 ± 0.09	4.93 ± 0.9	1.79 ± 0.3	0.29 ± 0.08
48[c]	1.07 ± 0.15	4.90 ± 0.4	1.10 ± 0.5	0.19 ± 0.03
51[b]	1.02 ± 0.15	5.62 ± 0.2	1.15 ± 0.3	0.23 ± 0.03
101[c]	1.19 ± 0.20	4.95 ± 0.2	1.30 ± 0.5	0.18 ± 0.04
104[b]	1.05 ± 0.17	5.26 ± 0.5	1.46 ± 0.4	0.17 ± 0.04
200[b]	0.96 ± 0.20	5.14 ± 0.6	1.8 ± 0.3	0.17 ± 0.05
302[b]	1.30 ± 0.04	5.76 ± 0.3	1.72 ± 0.7	0.15 ± 0.05
400[b]	1.33 ± 0.07	6.02 ± 0.5	1.32 ± 0.4	0.12 ± 0.05
451[b]	1.29 ± 0.04	5.62 ± 0.3	1.55 ± 0.5	0.12 ± 0.02
560[b]	1.42 ± 0.15	4.96 ± 1.0	1.42 ± 0.6	0.18 ± 0.06
612[b]	1.25 ± 0.15	6.07 ± 0.5	1.33 ± 0.4	0.18 ± 0.03
$T = 243$ K				
50[b]	1.50 ± 0.10	4.90 ± 0.5	1.30 ± 0.2	0.10 ± 0.04
$T = 313$ K				
56[b]	0.69 ± 0.08	5.54 ± 0.9	1.17 ± 0.1	0.24 ± 0.02
$T = 333$ K				
50[b]	0.83 ± 0.20	3.2 ± 1.5	0.95 ± 0.4	0.31 ± 0.04

[a] Presented are averages of values derived from experiments at different NO_2 concentrations ranging from 5×10^{14} to 6×10^{15} molecules cm^{-3}. Concentrations of DMDS and CH_3I were $(2-10) \times 10^{13}$ and $(1-5) \times 10^{13}$ molecules cm^{-3}, respectively. [b] Photolysis at 248 nm. [c] Photolysis at 351 nm.

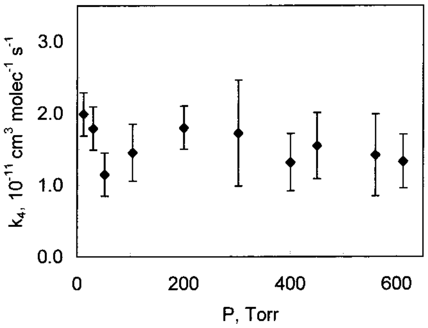

Figure 4. Pressure dependence of the second-order rate constant for the reaction of CH_3SO with NO_2 (4) at 300 K.

DMDS/NO_2 Photolysis. Numerical simulation of CH_3O concentration profiles was performed assuming several kinetic models of CH_3 formation: (a) formation of CH_3 in reaction 4b; (b) thermal decomposition of CH_3SO_2 (6) with production of CH_3SO_2 via reaction 4a; (c) formation of CH_3 in both reactions 4b and 6; (d) formation of CH_3 directly via reaction of CH_3SO_2 with NO_2 or indirectly via thermal decomposition of the CH_3SO_3 radical.

The fitting procedure of CH_3O profiles using model a was performed by varying only the rate coefficient k_4, while k_5 and k_9 were determined from the photolysis of CH_3I/NO_2 at the same NO_2 concentration as used in the DMDS/NO_2 mixtures. Reaction 4 was considered to proceed only via the channel 4b forming CH_3. Varying the branching ratio $\alpha_4 = k_{4b}/k_4$ would affect the calculated absolute concentration of CH_3O but not the shape of the CH_3O profile from which the total rate coefficient k_4 was determined. The rate constants k_4 obtained with this model did not exhibit any systematic dependence on NO_2 concentration and, as shown in Figure 1, provided a good description of the experimental profiles. The mean values of k_4 obtained at different pressures between 12 and 612 Torr from experiments carried out at different NO_2 concentrations are presented in Table 2 and Figure 4. These k_4 values are pressure independent within the given errors, yielding the average value $k_4 = (1.5 \pm 0.4) \times 10^{-11}$ cm^3 $molecule^{-1}$ s^{-1}.

Simulation of CH_3O profiles using model b required variation of two parameters, k_4 and k_6, and did not allow their independent determination, as might be expected. Within the accuracy of the experiments, the description of the CH_3O concentration profiles could be achieved using different combinations of k_4 and k_6. The lower limit of k_4 corresponds to the value found using model a, $k_4 \geq 1.5 \times 10^{-11}$ cm^3 $molecule^{-1}$ s^{-1}. To fit the calculated CH_3O profiles to the experimental ones, k_6 corresponding to the lower limit of k_4 has to be higher than $\sim 5 \times 10^6$ s^{-1}. In that case, reaction 4 is the limiting step of CH_3 formation. The lower limit of k_6 is conditioned by the accuracy of the experimental data.

The other limiting case, assuming fast reaction 4, provides an estimate of the lower limit for the rate of thermal decomposition (6). Increasing k_4 requires lowering k_6 with the limit value $k_6 = 5 \times 10^4$ s^{-1} reached at $k_4 \geq 5 \times 10^{-10}$ cm^3 $molecule^{-1}$ s^{-1}. However, the values of k_6 obtained by the fitting procedure at fixed k_4, $5 \times 10^{-10} \geq k_4 \geq 1.5 \times 10^{-11}$ cm^3 $molecule^{-1}$ s^{-1}, were found to be dependent on the NO_2 concentration, which is inconsistent with the assumed mechanism.

Similar results have been obtained using model c assuming CH_3 formation via both channels 4b and 6. The model requires $k_4 = 1.5 \times 10^{-11}$ cm^3 $molecule^{-1}$ s^{-1} and a fast thermal decomposition (6) with k_6 around the above limiting value, $k_6 = 5 \times 10^4$ s^{-1}, slightly dependent on the ratio k_{4b}/k_4. Another possibility with model c is to assume a slow decomposition of CH_3SO_2 via reaction 6, with a rate $k_6 \leq 100$ s^{-1}, combined with CH_3 formation in reaction 4b. The upper limit of k_6 in this case is determined by the characteristic time of the photolysis experiment and by the accuracy of the CH_3O profiles; at $k_6 \leq 100$ s^{-1} the fitted calculated CH_3O profiles are not sensitive to k_6.

Assuming model d, the rate of the CH_3 formation may be limited either by formation of CH_3SO_2 in reaction 4 or by formation of CH_3 in reactions 6−8. In both cases, the model requires unusually high rate constant for the faster step with the decomposition rates of CH_3SO_2 or CH_3SO_3 dependent on NO_2 concentration. In addition, the mechanism assuming SO_3 formation is inconsistent with the SO_2 formation observed by LIF and mass spectrometry in low-pressure experiments.

Summarizing the simulation results, we conclude that relative concentration profiles of CH_3O can be adequately described assuming formation of CH_3 in reaction 4 with $k_4 = (1.5 \pm 0.4)$

$\times 10^{-11}$ cm^3 molecule^{-1} s^{-1}. Nevertheless, the possibility of CH_3 formation via CH_3SO_2 decomposition (6) cannot be excluded provided that reaction 6 is either sufficiently fast, $k_6 \geq 5 \times 10^4$ s^{-1}, or very slow, $k_6 \leq 100$ s^{-1} in the pressure range used.

Yield of CH_3. The CH_3 yield has been determined by comparing the CH_3O concentration profiles obtained by photolysis of DMDS/NO_2 and CH_3I/NO_2 mixtures under the same experimental conditions. The CH_3O profiles obtained by photolysis of CH_3I/NO_2 were fitted by modeling using appropriate values for rate constants k_5 and k_9. These rate constant values were used to find the value of k_4 by model calculation by fitting the experimental CH_3O profiles from the photolysis of DMDS/NO_2. The yield of CH_3 has been derived from the ratio of integrals of the LIF signal over reaction time calculated using the determined rate constants k_5, k_9, and k_4.

Assuming direct formation of CH_3 radical in reaction 4b, the ratio of the integrals is related to the branching ratio $\alpha_4 = k_{4b}/k_4$ according to the following expression:

$$\alpha_4 = q\frac{([CH_3]_0 + \alpha_{10}\beta_{CH_3I}[O]_0^{CH_3I})}{([CH_3S]_0 + 2\beta_{DMDS}[O]_0^{DMDS})}\frac{\int_0^\infty I^{DMDS}\,dt}{\int_0^\infty I^{CH_3I}\,dt}$$

where I^{CH_3I} and I^{DMDS} are the time-dependent LIF signals intensities of CH_3O from the photolysis of CH_3I/NO_2 and DMDS/NO_2, respectively; q is a correction coefficient taking into account the different fluorescence quenching rates in the CH_3I/NO_2 and the DMDS/NO_2 mixtures; $[CH_3]_0$, $[CH_3S]_0$, $[O]_0^{DMDS}$, and $[O]_0^{CH_3I}$ are the initial radical concentrations produced by photolysis; $\alpha_{10} = k_{10a}/k_{10}$; $\beta_{CH_3I} = k_{10}[CH_3I]/k_{11}[NO_2]$ and $\beta_{DMDS} = k_3[DMDS]/k_{11}[NO_2]$ are coefficients accounting for the O atom consumption by NO_2:

$$O + NO_2 \rightarrow NO + O_2 \tag{11}$$

The above expression has been derived assuming the thermal decomposition (6) to be either much faster than reaction 4 or sufficiently slow to be negligible on the time scale of the experiments.

The integrals have been evaluated by numerical integration of calculated concentration profiles obtained by numerical simulation using the reaction scheme presented in Table 1. Reactions not included in Table 1, e.g., radical cross reactions, reactions with NO, and others, are of minor importance and do not influence the validity of the above equation. In fact, any other functional dependence giving statistically correct description of I^{CH_3I} and I^{DMDS} vs reaction time can be used for the integral evaluation and, provided such description, the value of α_4 obtained using this procedure is not sensitive to the rate constants used to calculate the integrals.

The ratio in the expression for α_4 containing radicals and O atom initial concentrations was evaluated from the initial concentrations of CH_3I, DMDS, and NO_2 using known photolysis cross sections at 248 nm; $\sigma^{CH_3I} = 7.73 \times 10^{-19}$,[31] $\sigma^{DMDS} = 1.243 \times 10^{-18}$,[32] and $\sigma^{NO_2} = 2.75 \times 10^{-20}$,[33] in units of cm^2 molecule^{-1}:

$$\frac{([CH_3]_0 + \alpha_{10}\beta_{CH_3I}[O]_0^{CH_3I})}{([CH_3S]_0 + 2\beta_{DMDS}[O]_0^{DMDS})} = \frac{(\sigma^{CH_3I}[CH_3I] + \alpha_{10}\beta_{CH_3I}\sigma^{NO_2}[NO_2])}{(2\sigma^{DMDS}[DMDS] + 2\beta_{DMDS}\sigma^{NO_2}[NO_2])}$$

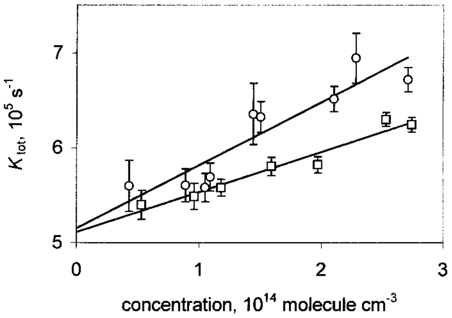

Figure 5. Dependencies of total CH_3O fluorescence quenching rate K_{tot} vs concentration of CH_3I (○) and DMDS (□) at $P = 103.7$ Torr and $[NO_2] = 5 \times 10^{14}$ molecules cm^{-3}.

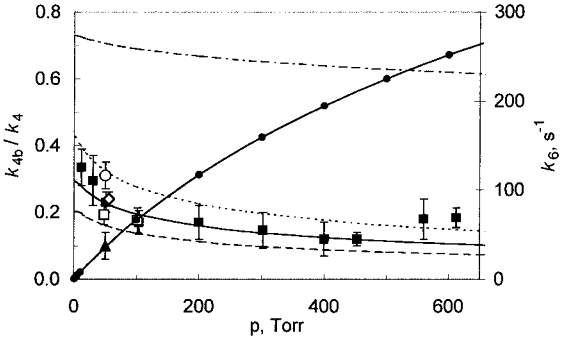

Figure 6. Calculated pressure dependence for the thermal CH_3SO_2 decomposition rate coefficient (solid line with points) and pressure dependencies of CH_3 yield: (○), (◇), (■), (△) 248 nm photolysis at T = 333, 313, 300, and 243 K, respectively; (□) 351 nm photolysis at 300 K. Pressure dependencies of CH_3SO_2* prompt decomposition fraction α_{12} calculated using $E^* = 13.44$, 13.72, 14.09 kcal/mol and thermal distribution with $\langle E \rangle = 16.9$ kcal/mol are presented by dashed, solid, dotted, and dotted–dashed lines, respectively.

As the laser fluence was the same during the experiments with the two reaction mixtures, the value corresponding to this term is independent of the photolysis laser fluence.

The coefficient accounting for different rates of fluorescence quenching by CH_3I and DMDS has been estimated using the following expression:

$$q = \left(\frac{K_{tot}^{DMDS}}{K_{tot}^{CH_3I}}\right)^2 \exp\{(K_{DMDS} - K_{CH_3I})t_0\}$$

where K_{tot}^{DMDS} and $K_{tot}^{CH_3I}$ are the total fluorescence quenching rates in DMDS/NO_2 and CH_3I/NO_2 mixtures; K_{DMDS} and K_{CH_3I} are the quenching rates by DMDS and CH_3I, respectively, $K_{DMDS} = k_{DMDS}[DMDS]$ and $K_{CH_3I} = k_{CH_3I}[CH_3I]$; $t_0 = 100$ ns is the delay between the probing laser pulse and the start of LIF signal integration.

The fluorescence quenching rates, K_{tot}, were determined from the CH_3O fluorescence decay rates, which were exponential. $k_{DMDS} = (7 \pm 2) \times 10^{-10}$ cm^3 molecule^{-1} s^{-1} and $k_{CH_3I} = (4.2 \pm 0.8) \times 10^{-10}$ cm^3 molecule^{-1} s^{-1} have been derived from the slope of the straight lines obtained by plotting K_{tot} vs CH_3I and DMDS concentrations, as shown in Figure 5. The maximal correction for quenching corresponded to the lowest NO_2 concentrations and was about 10%.

The yield of CH_3 has been found to be independent of the NO_2 concentration and it exhibited a pressure dependence varying from 0.33 at 12 Torr to 0.18 at 612 Torr, as shown in Figure 6 and Table 2. Each point represents an average of 5–10 measurements performed at different NO_2 concentrations ranging from 5×10^{14} to 6×10^{15} molecules cm^{-3}.

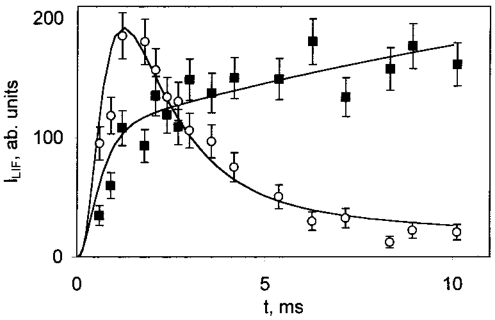

Figure 7. Kinetics of SO_2 (■) and CH_3O (○) obtained in a discharge flow experiment at 1 Torr pressure of He and $[NO_2] = 3.46 \times 10^{14}$ molecules cm^{-3}. Solid lines are the calculated dependencies obtained with $\alpha_4 = 0.4$ and $k_6 = 57$ s^{-1}.

The branching ratio α_4 obtained from the 248 nm photolysis data is based on the assumption of unity yields of CH_3 and CH_3S from the photolysis of CH_3I and DMDS, respectively. To verify this assumption, some experiments were performed by photolyzing DMDS/NO_2 and CH_3I/NO_2 mixtures at 351 nm. In this case, the photolysis of DMDS and CH_3I is negligible compared to that of NO_2 and CH_3 and CH_3S are formed in reactions 10 and 3, respectively. The relation between the fluorescence intensity integrals and branching ratio α_4 is given by the following expression, which also accounts for the equal initial concentrations of O atoms in both reaction mixtures:

$$\alpha_4 = q\frac{\alpha_{10}k_{10}[CH_3I]}{2k_3[DMDS]}\frac{\int_0^\infty I^{DMDS}\,dt}{\int_0^\infty I^{CH_3I}\,dt}$$

As presented in Figure 6, the values of α_4 derived from the photolysis at 248 nm and at 351 nm are in good agreement, which validates the assumed reaction mechanism and provides indirect confirmation for the values α_{10}, k_{10}, k_3, and photolysis cross sections used in this study.

The yield of CH_3 in reaction 4, α_4, has been found to be temperature dependent. As presented in Figure 6 and Table 2, at a pressure of 50 Torr, α_4 increases from 0.1 ± 0.04 at 243 K to 0.31 ± 0.04 at 333 K.

Discharge Flow − MS/LIF Results. Formation of both SO_2 and CH_3O has been observed in the discharge flow experiments at a pressure of 1 Torr in agreement with the previous study from this laboratory.[11] At short reaction times, the LIF signal was a superposition of CH_3O and SO_2 fluorescence, while the fluorescence excitation spectra could be represented as their weighted sum. At long reaction times, the LIF excitation spectra were those of SO_2 only.

Typical reaction time dependencies of SO_2 and CH_3O LIF signals are presented in Figure 7. Similarly to the results obtained in the photolysis experiments, the concentration profiles of SO_2 and CH_3O exhibit a fast initial increase in agreement with the mechanism assuming formation of CH_3 and SO_2 in reaction 4b. A slower increase of SO_2 concentration is observed at longer reaction times, and the kinetics of SO_2 formation could be divided in three distinct regions: a fast initial generation, a much slower one at longer reaction times, and a quasistationary part where the concentration of SO_2 was independent of reaction time.

Observed behavior of SO_2 kinetic profiles could be adequately described with the mechanism including two different SO_2 formation routes: fast formation of SO_2 together with CH_3 in reaction 4b and slow unimolecular decomposition of the CH_3SO_2 radical produced in reaction 4a. The branching ratio $\alpha_4 = k_{4b}/k_4$ and decomposition rate constant k_6 were determined by fitting calculated SO_2 profiles with simultaneous optimization of both parameters. The most important reactions included in the model were the reaction CH_3SH + Cl forming CH_3S and reactions 2, 4, and 6. Since α_4 and k_6 influence different parts of the SO_2 profile, their unambiguous determination using simultaneous optimization was quite possible and provided unique combinations of the parameters. The resulting average values are $\alpha_4 = (0.4 \pm 0.2)$, which is in good agreement with the photolysis results extrapolated to low pressure (Figure 6), and $k_6 = (50 \pm 30)$ s^{-1}.

TABLE 3: SO_2 Yield in the Cl/CH_3SH/NO_2 Reaction System at 1 Torr of He and T = 300 K

$[NO_2]$, 10^{14} molecule cm^{-3}	$[Cl]_0$, 10^{11} molecule cm^{-3}	α_{SO_2}
1.44	6.25	0.98
2.0	0.375	0.99
2.22	0.375	1.23
5.0	0.73	0.86
7.4	1.5	1.12
7.85	0.375	1.11
8.6	6.5	0.81
8.6	1.5	1.05
10.5	6.5	1.00
12.5	1.5	1.26
15.3	0.375	0.85
17.2	6.8	1.00
21	6.8	0.9
26	6.92	0.92
49.8	1.5	1.01

The "slow" SO_2 generation process observed in the experiment at long reaction times may be also explained by wall decomposition of the CH_3SO_2 radical with releasing of SO_2 to the gas phase. As we could not distinguish between gas-phase and heterogeneous SO_2 generation, the value of k_6 given above should be considered as an upper limit for the gas-phase thermal decomposition of CH_3SO_2 at 1 Torr of He, $k_6 \leq (50 \pm 30)$ s^{-1}.

The absolute SO_2 yield was measured as the ratio of SO_2 concentration at long reaction times corresponding to the quasistationary part of the SO_2 concentration profiles to the initial Cl atom concentration, $\alpha_{SO_2} = [SO_2]_\infty/[Cl]_0$. As shown in Table 3, the measured yield was independent of NO_2 concentration in the investigated range, $[NO_2] = (0.14-5) \times 10^{15}$ molecules cm^{-3} with an average yield close to unity: $\alpha_{SO_2} = (1.01 \pm 0.1)$. Unity yield of SO_2 indicates that at a pressure of 1 Torr of He the reaction of CH_3SO with NO_2 proceeds predominantly via channels 4a and 4b, leading to SO_2 formation.

Assuming reaction 4b and CH_3SO_2 decomposition (6) or wall decomposition to be the only sources of SO_2 and reaction with NO_2 (7) to be the only other consumption channel of CH_3SO_2 in the system, we obtain $k_7[NO_2]/k_6 \leq 0.1$ based on the independence of SO_2 yield on NO_2 concentration. The upper limit of 0.1 for the $k_7[NO_2]/k_6$ ratio is determined by the accuracy of the α_{SO_2} value estimated accounting for a 2σ statistical error in measurement of SO_2 LIF signal intensities and calibration of Cl and SO_2. Using an upper limit of 50 s^{-1} for k_6 derived from these experiments we obtain $k_7 \leq 1 \times 10^{-15}$ cm^3 $molecule^{-1}$ s^{-1} from the highest NO_2 concentration used ($[NO_2] = 5 \times 10^{15}$ molecules cm^{-3}).

To describe the fast increase and decay parts of the experimental CH_3O profiles, it was also necessary to include two different CH_3 forming routes in the model. Nevertheless, because of the dominant contribution of SO_2 fluorescence at reaction times corresponding to the decay part of CH_3O concentrations profiles, an unambiguous determination of k_6 and α_4 from CH_3O profiles was not possible. We can only conclude

TABLE 4: Relative Energies (in kcal/mol) and ZPE Corrected Total Energies (in Hartrees) of Stationary Points on Potential Energy Surface of the CH_3SO_2 Decomposition

	CH_3SO_2	$[CH_3-SO_2]^*$	CH_3	SO_2	$CH_3 + SO_2$
B3LYP/6-31+G*	−588.42947		−39.81334	−548.59281	−588.40615 (14.63)[a]
B3LYP/6-311+G**	−588.50567		−39.82610	−548.65831	−588.48441 (13.34)
MP2/6-31G*	−587.34672	−587.32376 (14.41)[a]	−39.64352	−547.69376	−587.33728 (5.93)
MP2/6-311G**	−587.63217	−587.61016 (13.81)	−39.69626	−547.92671	−587.62297 (5.77)
G2	−587.78423	−587.76317 (13.22)	−39.74509	−548.01574	−587.76083 (14.69)
G2//MP2(ZPE = MP2)	−587.78482	−587.76244 (14.04)	−39.74409	−548.01829	−587.76238 (14.08)
G2//QCI	−587.78403		−39.74506	−548.01772	−587.76278 (13.33)

[a] Energies in kcal/mol relative to energy of CH_3SO_2.

TABLE 5: Relative Energies (in kcal/mol) and ZPE Corrected Total Energies (in Hartrees) of Stationary Points on the Potential Energy Surface of the $CH_3SO + NO_2$ Reaction

	CH_3SO	NO_2	$CH_3S(O)ONO$	NO	$CH_3SO_2 + NO$
B3LYP/6-31+G*	−513.24409	−205.07528	−718.33814 (−11.78)[a]	−129.89105	−718.32052 (−0.72)[a]
G2	−512.65961	−204.83686	−717.54001 (−27.32)	−129.73995	−717.52418 (−17.38)

[a] Energies in kcal/mol relative to energy of $CH_3SO + NO_2$.

that the experimental CH_3O concentration profiles qualitatively agree with the above proposed mechanism.

Theoretical Study

According to the experimental results of this work, the reaction of CH_3SO with NO_2 would proceed predominantly via the two reaction channels forming CH_3SO_2 (4a) and $CH_3 + SO_2$ (4b). Considering both the weak negative pressure dependence of CH_3 yield and pressure independence of k_4 observed in this study, the following mechanism including formation of chemically activated $CH_3SO_2^*$ is suggested:

$$CH_3SO + NO_2 \rightarrow CH_3S(O)ONO^* \rightarrow CH_3SO_2^* + NO \quad (4c)$$

$$CH_3SO_2^* \rightarrow CH_3 + SO_2 \quad (12a)$$

$$CH_3SO_2^* + He \rightarrow CH_3SO_2 + He \quad (12b)$$

The chemically activated $CH_3SO_2^*$ may undergo either a prompt decomposition to CH_3 and SO_2 (12a) or a collisional stabilization (12b) followed by thermal decomposition (6).

To validate the above mechanism and to verify its consistency with experimental results, a computational study has been performed, in which RRKM theory has been used for the calculation of the $CH_3SO_2^*$ prompt decomposition to stabilization rates ratio and of the CH_3SO_2 thermal decomposition rate.

Reaction Path Calculations for the CH_3SO_2 Decomposition and the $CH_3SO + NO_2$ Reaction. Ab initio and DFT calculations have been performed using the GAUSSIAN 94 program package.[34]

The geometries of species relevant to the CH_3SO_2 decomposition were optimized on the MP2 level and using the DFT B3LYP model. The energies were calculated using G2 theory which provides the energies at effectively the QCISD(T)/6-311+G(3df,2p) level for the equilibrium geometries obtained at the MP2(Full)/6-31G(d) level and with zero-point energies (ZPE) obtained from HF/6-31G(d) frequencies. To estimate the influence of the different equilibrium geometries, the energies were also calculated using G2//MP2(ZPE=MP2) and G2//QCI variations of G2 theory. In G2//MP2(ZPE=MP2), the geometries and ZPE are calculated at MP2(full)/6-311G(d,p) level. The ZPE are scaled by 0.9748.[35] In G2//QCI, the geometry is obtained at the QCISD/6-31G(d) level.[36] The results of the calculations are presented in Tables 4 and 5.

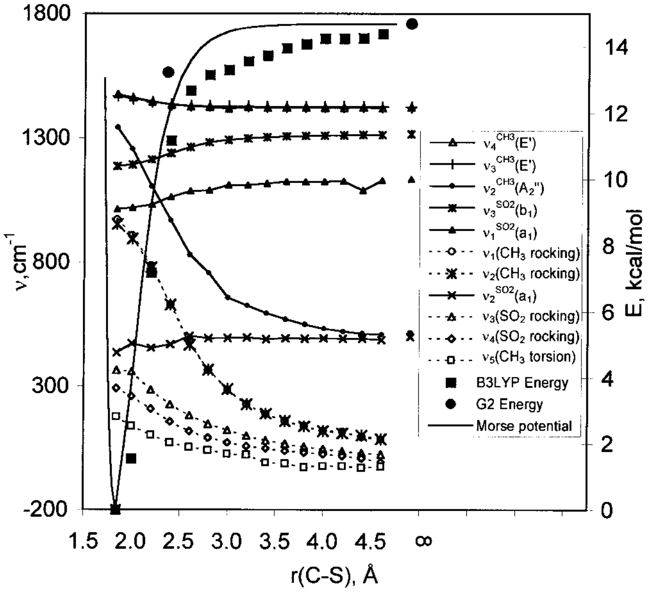

Figure 8. G2 and ZPE corrected B3LYP/6-31+G(d) relative energies and B3LYP/6-31+G(d) vibrational frequencies along the reaction path for the dissociation of the CH_3SO_2 radical.

The geometries of the stable CH_3SO_2 radical optimized on MP2 and B3LYP are very similar, the B3LYP C−S bond length, ∼0.03 Å longer. The geometries are identical to those reported earlier,[37,38] which were optimized using MP2 and B3LYP with 6-311G(d,p) and 6-31+G(2d,p) basis sets.

The G2 energy of CH_3SO_2 relative to $CH_3 + SO_2$ is −14.69 kcal/mol. Using the geometries optimized at MP2 and QCISD levels slightly lowers this energy difference to −14.08 and −13.33 kcal/mol, respectively. The G2(MP2) dissociation energy of CH_3SO_2 has been reported to be 14.1 kcal/mol in the very recent paper of Frank and Turecek.[38]

The transition state for the CH_3SO_2 decomposition has been located on MP2 level and corresponds to a C−S bond length of 2.36 Å for both basis sets 6-31G* and 6-311G**. No saddle point has been found using the B3LYP model with both basis sets 6-31+G* and 6-311+G**. As shown in Figure 8, the B3LYP energies steadily increase with the separation of CH_3 and SO_2 fragments reaching at the large r(C−S) the sum of CH_3 and SO_2 energies. Also, G2 energies corresponding to the MP2 geometry of the transition state are lower than the dissociation energies calculated at the same level, indicating that in accordance with B3LYP results the reaction path for

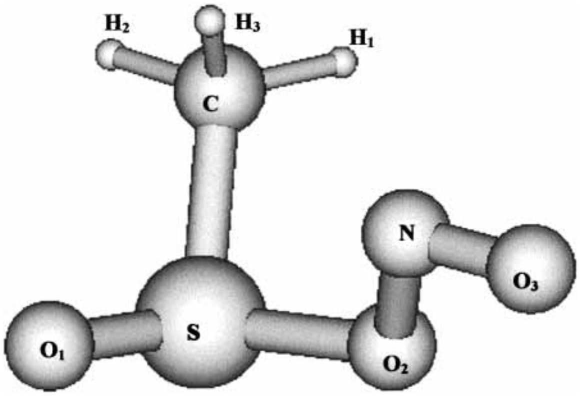

Figure 9. Stable $CH_3S(O)ONO$ intermediate along the $CH_3SO + NO_2$ reaction path. B3LYP/6-31+G(d) and MP2/6-31+G(d) geometry: $r(C-S) = 1.83(1.81)$, $r(S-O_2) = 1.74(1.70)$, $r(N-O_2) = 1.48(1.60)$, $r(N-O_3) = 1.17(1.17)$, $r(S-O_1) = 1.49(1.49)$, $r(C-H_3) = 1.092(1.091)$, $r(C-H_1) = 1.093(1.092)$, $r(C-H_2) = 1.094(1.093)$, $A(C-S-O_1) = 106.07(105.4)$, $A(O_1-S-O_2) = 110.24\ (110.87)$, $A(S-O_2-N) = 114.61(112.21)$, $A(O_2-N-O_3) = 109.49(108.82)$, $A(H_3-C-S) = 109.32(109.32)$, $A(H_2-C-S) = 109.17(106.88)$, $A(H_1-C-S) = 109.28(109.47)$, $D(C-S-O_1-O_2) = 103.9(104.00)$, $D(O_1-S-O_2-N) = -53.83(-51.35)$, $D(O_3-N-O_2-S) = 174.27(171.24)$, $D(O_2-S-C-H_3) = -66.12(-67.29)$, $D(O_2-S-C-H_1) = 56.23(55.07)$, $D(O_2-S-C-H_3) = 175.23\ (174.4)$.

the CH_3SO_2 decomposition has no chemical barrier, although on G2(MP2) a small barrier for the recombination, 0.3 kcal/mol, has been reported.[38]

The exoergicity of reaction 4a on the G2 level is -17.38 kcal/mol. In contrast with the results obtained for the CH_3-SO_2 system, the exoergicity calculated on the B3LYP level, -0.72 kcal/mol, is quite different from the G2 result.

A stable intermediate, $CH_3S(O)ONO$, has been located at the HF level, and its geometry has been optimized on MP2/6-31+G(d) and B3LYP with 6-31+G(d) and 6-311+G(d,p) basis sets. As presented in Figure 9, the structures optimized on MP2 and B3LYP are similar. The G2 energy of the stable intermediate is -27.3 kcal/mol relative to $CH_3SO + NO_2$.

Adopting the G2 energies for both $[CH_3SO-NO_2]$ and $[CH_3-SO_2]$ systems, we come to the mechanism in which the reaction of CH_3SO proceeds via the stable intermediate $CH_3S(O)ONO$. Possessing 27.32 kcal/mol excess energy compared to ~10 kcal/mol dissociation energy, the $CH_3S(O)ONO$ intermediate is likely to decompose promptly with formation of activated CH_3SO_2. Assuming the decomposition of $CH_3S(O)ONO$ to be sufficiently fast to neglect collisional energy transfer, the CH_3SO_2 radical will possess the excess energy determined by the exoergicity of the reaction 4a, $\Delta E_{4a} = -17.38$ kcal/mol, by the activation barrier of the entrance channel and by the thermal energy of the entrance transition state corresponding to the formation of $CH_3S(O)ONO$. The B3LYP energy calculations performed in this work for the $CH_3S(O)ONO$ geometries optimized at different fixed $r(S-O_2)$ bond lengths showed continuous increase of the energy with increasing of $r(S-O_2)$ and in the following calculations we assume the potential surface for the entrance channel to possess no barrier. Assuming also the thermal energy to be determined by the number of vibrational degrees of freedom, 21 for $CH_3S(O)ONO$, and the energy partitioning according to the degrees of freedom numbers ratio, the available energy for the CH_3SO_2 may be estimated to be $15/21 \times (17.38 + (21 \times 0.3)) = 16.9$ kcal/mol, which is about 2.2 kcal/mol higher than the CH_3SO_2 dissociation energy, $E_d = 14.69$ kcal/mol.

Thermal Decomposition of the CH_3SO_2 Radical. The RRKM calculations for the thermal decomposition of CH_3SO_2 were performed using the UNIMOL program suite.[39] The position of the transition state along the reaction path was determined by minimization of the high-pressure rate coefficient according to the canonical variational transition state theory (CVTST).[40]

The microcanonical rate coefficients $k(E,J)$ were computed accounting for angular moment conservation using the modified Beyer−Swinehart method for calculating rovibrational density of states.[41] Rotational constants and projected vibrational frequencies along the reaction path have been calculated at the B3LYP/6-31+G(d) level with the step 0.2 Å, as shown in Figure 8. The potential energy was represented by a Morse potential with D_e corresponding to the G2 dissociation energy 14.69 kcal/mol and $\beta = 5.77$ Å^{-1} chosen as a compromise between the G2 and B3LYP energies.

The angular momentum corresponding to the two-dimensional external rotations about the two axis approximately perpendicular to the C−S bond was considered to be conserved and the corresponding rotational energy was accounted for by calculating the effective critical energy at the position of centrifugal barrier on the effective potential along the reaction path. One external rotation, approximately around C−S bond was considered to be active. A torsional CH_3 motion was treated as free rotation with rotational constant of free CH_3 radical. The rocking of SO_2 fragment was considered as a vibration, except for the C−S bond longer than 2.8 Å, where these motions were considered as free rotations.

At $T = 300$ K, the high-pressure rate coefficient has been found by variational procedure to be $k_6^\infty = 2.08 \times 10^3\ s^{-1}$ with the transition state located at $r(C-S) = 2.6$ Å. This value corresponds to the high-pressure A factor, $A_\infty = 10^{14.48}\ s^{-1}$, and high-pressure activation energy, $E_\infty = 15.32$ kcal/mol:

$$k_6^\infty(300K) = 10^{14.48} \exp(-15320/RT)$$

The high-pressure rate coefficient obtained by Frank and Turecek[38] using RRKM calculations with G2(MP2) energies and transition state located at $r(C-S) = 2.415$ Å is 2 times lower.

Falloff calculations for the thermal decomposition of CH_3SO_2 were performed using the UNIMOL program suite.[39] For the collisional vibrational energy transfer, the exponential model has been used with estimated average energy transfer per CH_3SO_2-He collision $\langle \Delta E_{down} \rangle = 150\ cm^{-1}$ and Lennard-Jones collisional parameters estimated[40] to be $\sigma_{CH_3SO_2-He} = 3.8$ Å and $\epsilon_{CH_3SO_2-He} = 50$ K. For the rotational energy transfer a strong collision model has been adopted.

The calculated pressure dependence of k_6 at 300 K is presented in Figure 6. At 1 and 760 Torr of He, the rate coefficients are 1.0 s^{-1} and 285 s^{-1}, respectively. The low-pressure rate coefficient has been found to be $k_6^0 = 2.72 \times 10^{-17}\ cm^3\ molecule^{-1}\ s^{-1}$. Using the above values for k_6^0 and k_6^∞, the calculated k_6 may be presented by Troe expression with $F_{cent} = 0.5$ for the pressure range from 1 Torr to 760 Torr of He (Figure 6).

The calculated rate constants for the thermal decomposition of CH_3SO_2 are in reasonable agreement with experimentally estimated values of $k_6 < 100\ s^{-1}$ at pressures of 20−600 Torr and $k_6 < 50\ s^{-1}$ at a pressure of 1 Torr. It should be noted that the falloff behavior is very sensitive to the values of collisional parameters which have been only roughly estimated for the present calculations. Considering the weakness of the CH_3-SO_2 bond, the value of $\langle \Delta E_{down} \rangle$, which is dependent on the internal excitation energy, may be significantly lower and, as a consequence, the calculated k_6 will be also lower, giving better agreement with experimental results. Also, it should be mentioned, that the calculated rate constant is strongly dependent on the critical energy used. As the expected accuracy of the presented G2 values is likely to be not better than 1 kcal/mol, the calculated rate constants should be considered only as a rough estimation.

Prompt Decomposition of Chemically Activated CH_3SO_2. The fraction of chemically activated CH_3SO_2 radicals undergoing prompt decomposition has been determined by solving the master equation describing time evolution of the CH_3SO_2 energy distribution function. The master equation was solved numerically using the BDF method implemented in the D02EJF routine of NAG Fortran Library. The *J*-averaged microcanonical rate coefficients $k(E)$ and energy transfer probabilities were calculated as described above using the MAS55 program[39] with modified output.

The evolution of the distribution function is dependent on the initial energy distribution and determined by the competition between collisional energy relaxation and loss via decomposition to $CH_3 + SO_2$ products. The prompt decomposition proceeds within less than 10^{-7} s and is followed by relaxation of the initial energy distribution to quasithermal distribution on the time scale $10^{-7}-10^{-5}$ s, depending on pressure. The fraction of prompt decomposition was determined from the ratio of integrals of distribution functions over energy at $t \approx 10^{-6}$ s and at $t = 0$, $\alpha_{12} = k_{12a}/k_{12} = 1 - \sum f_{t\approx 10^{-6}}(E_i)/\sum f_0(E_i)$. The pressure dependence of the fraction has been calculated for various initial energy distributions, and the obtained results are presented in Figure 6 together with the experimental data.

The critical parameters determining the calculated α_{12} values are the energy E^* assumed to be deposited in $CH_3SO_2^*$ and the effective critical energy for the CH_3SO_2 decomposition, E_0^{eff}. The E_0^{eff} was calculated using the G2 result for dissociation energy $E_0 = 14.69$ kcal/mol. With accounting for angular moment conservation, the effective critical energy is pressure dependent and, assuming thermal rotation energy distribution, the E_0^{eff} varies from 12.88 kcal/mol at 1 Torr to 13.17 kcal/mol at 760 Torr of He.

The influence of the E^* on the calculated prompt decomposition fraction has been derived using the initial distribution in the form of the δ function $f(E_i - E^*) = 1$ with different E^*. Also, the solution has been obtained, using the initial energy distribution calculated assuming that E^* is the sum of $-\Delta E_{4a} = 17.38$ kcal/mol and the part of thermal energy, distributed among $CH_3SO_2^*$, NO and their relative motion according to the energy dependence of the combined density of states.[42] The resulting initial distribution function is centered at $E = 16.9$ kcal/mol and has a width of about 8 kcal/mol. The results of these calculations, presented in Figure 6, show a strong dependence of the calculated prompt decomposition fraction on the initially available energy E^*, while the pressure dependence is not very sensitive to the form of initial energy distribution. Assuming that total energy released in reaction 4a is deposited on the exited CH_3SO_2 radical leads to the fraction of prompt decomposition from 0.73 at 1 Torr to 0.61 at 760 Torr of He. Good agreement with the experimental results is reached using $E^* = 13.7$ kcal/mol. The calculated pressure dependence reproduces well the experimental one. Also, the experimental temperature dependence is in qualitative agreement with the model. The value $E^* = 13.7$ kcal/mol is 3.2 kcal/mol lower than estimated above as available for CH_3SO_2. Nevertheless, considering the assumptions made about the form of potential surface along the $CH_3SO + NO_2$ reaction path and accounting for the accuracy of G2 calculations, about 1.5 kcal/mol, the prompt decomposition fraction calculations may be considered as consistent with experimental results of the present work.

Discussion

The reaction of CH_3SO with NO_2 (4) has been studied by monitoring kinetics and absolute yields of CH_3O and SO_2 in the pressure range from 1 to 612 Torr of He. The reaction rate constant $k_4 = (1.5 \pm 0.4) \times 10^{-11}$ cm^3 molecule^{-1} s^{-1} has been found to be independent of pressure in the pressure range used in this study. On the basis of the observed pressure dependence of CH_3O yield and unity yield of SO_2 at 1 Torr of He, reaction 4 has been suggested to proceed predominantly via the channel forming chemically activated CH_3SO_2 radical with 20% of prompt decomposition to CH_3 and SO_2 at 300 K and 1−612 Torr of He pressure. This mechanism has been validated theoretically by ab initio calculations.

Formation of thermalized CH_3SO_2 has not been directly observed in this study. Nevertheless, assuming the validity of the suggested mechanism, the CH_3SO_2 decomposition rate at $P = 1-612$ Torr of He has been estimated to be less than 100 s^{-1} which is in fair agreement with the RRKM calculations carried out.

Comparison with Previous Studies. The rate coefficient k_4 has been derived in the present study by least-squares fitting of calculated and experimental CH_3O profiles varying only one parameter, the rate coefficient k_4. Within the limits of experimental error, the obtained value, $k_4 = (1.5 \pm 0.4) \times 10^{-11}$ cm^3 molecule^{-1} s^{-1}, is consistent with the only direct mass spectrometric measurement of Dominé et al. $k_4 = (1.2 \pm 0.25) \times 10^{-11}$ cm^3 molecule^{-1} s^{-1}.[17]

The CH_3SO_2 thermal decomposition was studied by Ray et al.[11] at 0.75 Torr of He using the discharge flow technique similar to that of the present work. Disagreement between their rate coefficient $k_6 = (510 \pm 150)$ s^{-1} [11] and the upper limit $k_6 \leq 100$ s^{-1} experimentally derived in the present work may come from the fitting procedure used by Ray et al.[11] The coefficient k_6 was derived from fitting of experimental SO_2 and CH_3O profiles with simultaneous variation of k_6 and k_7 coefficients. However, further analysis of the experimental data of Ray et al.[11] shows that, as a rule, these two parameters cannot be uniquely resolved and a statistically acceptable description can be obtained with several combinations of varying parameters. The result of this analysis is qualitatively the same as that presented in the Experimental Results section of the present work. Furthermore, the experimental curves of Ray et al.[11] could also be simulated using the model suggested in this work, including two sources of SO_2, i.e., prompt decomposition of $CH_3SO_2^*$ formed in (4) and slow formation possibly on the surface of the reactor. Also, scattering of the parameters extracted from the data of ref 11 was large, which may be explained by inaccurate correction for the contributions of LIF signals of CH_3O and SO_2 to that of SO_2 and CH_3O, respectively. The above discussion gives tentative but not definitive explanation for the disagreement between the two studies. It is noteworthy, that the present results for the rate of CH_3SO_2 thermal decomposition are consistent with those of an earlier discharge flow study of $Cl/CH_3SH/NO_2$ mixtures from the same group.[43] The decomposition rate $k_6 \leq 10$ s^{-1} at 0.3 Torr of He was estimated from the mass spectrometric kinetics at the SO_2^+ peak corresponding to the contribution of both CH_3SO_2 and SO_2.

Besides, NO has been identified by Tyndall et al.[18] as a product of reaction 4 with about unity yield. The total yield of NO from the photolysis of DMDS/NO_2 mixture at 248 nm has been found to be about 2. This is consistent with the conclusion of the present work about the formation of CH_3SO_2 radical, stable on the time scale of photolysis experiment, and a yield of only about 0.2 for CH_3 formation in reaction 4. Considering this latter result and assuming unity yields of NO in reactions 4 and 2 and ~0.5 yield of NO in reaction of CH_3 with NO_2 at a pressure of 300 Torr used in ref 18, the total NO yield should be about 2.1 in the DMDS/NO_2 photolysis. In contrast, the fast thermal CH_3SO_2 decomposition assumed by Ray et al.[11] would lead to higher NO yield.

Atmospheric Implications. The results from this work provide some information about SO_2 formation and yield in the atmospheric oxidation of DMS. First of all, the results suggest the possible existence of a new formation route of SO_2, namely the prompt decomposition of excited CH_3SO_2, while the thermal decomposition of CH_3SO_2 has been the only source of SO_2 considered so far.

The direct atmospheric application of the present study concerns NO_x rich coastal areas where the reaction $CH_3SO + NO_2$ (4) can be the major or at least a significant oxidation pathway of CH_3SO in the DMS oxidation. The present results suggest that the SO_2 yield from reaction 4 would be at least on the order of 10−20% corresponding to the branching ratio of reaction 4b at atmospheric pressure. The contribution of the thermal decomposition of CH_3SO_2 will depend on reaction rates of reaction 6 and reactions of CH_3SO_2 with oxidants such as NO_2 and O_3. Then a better definition of k_6 and the determination of k_7 and $k(CH_3SO_2 + O_3)$ are needed to estimate the contribution of reaction 6 to the SO_2 yield in reaction of CH_3SO with NO_2.

The indirect application of the results presented here is for a remote marine atmosphere where the SO_2/aerosol formation from DMS is more important for the climate issue since DMS may be the major source of CN and CCN. In such a low NO_x atmosphere, the CH_3SO oxidation by NO_2 will be negligible compared to, e.g., oxidation by ozone. The data obtained for the $CH_3SO + NO_2$ reaction suggest that prompt CH_3SO_2 decomposition mechanism may also occur in the $CH_3SO + O_3$ reaction

$$CH_3SO + O_3 \rightarrow CH_3SO_2{}^* + O_2 \rightarrow CH_3 + SO_2 + O_2 \quad (13a)$$

$$CH_3SO + O_3 \rightarrow \text{products} \quad (13b)$$

The enthalpy of the reaction forming CH_3SO_2 is about 48 kcal/mol higher for the reaction $CH_3SO + O_3$ compared to $CH_3SO + NO_2$. If the mechanisms of CH_3SO reactions with O_3 and NO_2 are similar, the yield of SO_2 from the prompt decomposition of $CH_3SO_2{}^*$ formed in (13a) may be higher than from reaction with NO_2. Then, data are specially needed on the rate and mechanism of reaction of CH_3SO with O_3 to better define the SO_2 yield in the atmospheric oxidation of DMS, this yield being a key parameter in assessing the role of DMS in CN and CCN formation in relation to climate.

Acknowledgment. The authors gratefully acknowledge financial support of this work from the European Commission within Environmental Program (DOMAC project) and computer time granted by Institut du Développement et des Ressources en Informatique Scientifique (IDRIS).

References and Notes

(1) Andreae, M. O. In *The Role of Air Sea Exchange in Geochemical Cycling*; Buat-Menard, P., Reidel, D., Eds.; Kluwer Academic Publishers: Norwell, MA, 1986; p 331.

(2) Charlson, R. J.; Lovelock, J. E.; Andreae, M. O.; Warren, S. G. *Nature* **1987**, *326*, 655.

(3) Hynes, A. J.; Wine, P. H.; Semmes, D. H. *J. Phys. Chem.* **1986**, *90*, 4148.

(4) Butkovskaya, N. I.; Le Bras, G. *J. Phys. Chem.* **1994**, *98*, 2582.

(5) Patroescu, I. V.; Barnes, I.; Becker, K. H.; Mihalopoulos, N. *Atmos. Environ.* **1999**, *33*, 25.

(6) Sorensen, S.; Falbe-Hansen, H.; Mangoni, M.; Hjorth, J.; Jensen, N. R. *J. Atmos. Chem.* **1996**, *100*, 8895.

(7) Berresheim, H.; Wine, P.; Davis, D. In *Composition, Chemistry, and Climate of the Atmosphere*; Singh, H., Ed.; Van Nostrand Reinhold: New York, 1995; p 251.

(8) Barone, S. B.; Turnipseed, A. A.; Ravishankara, A. R. *Faraday Discuss.* **1995**, *100*, 39.

(9) Turnipseed, A. A.; Barone, S. B.; Ravishankara, A. R. *J. Phys. Chem.* **1992**, *96*, 7502.

(10) Urbanski, S. P.; Stickel, R. E.; Wine, P. H. *J. Phys. Chem. A* **1998**, *102*, 10522.

(11) Ray, A.; Vassalli, I.; Laverdet, G.; Le Bras, G. *J. Phys. Chem.* **1996**, *100*, 8895.

(12) Mellouki, A.; Téton, S.; Laverdet, G.; Quilgars, A.; Le Bras, G. *J. Chim. Phys.* **1994**, *91*, 473.

(13) Nicovich, J. M.; Wang, S.; Wine, P. H. *Int. J. Chem. Kinet.* **1995**, *27*, 359.

(14) Park, J.-Y.; Slagle, I. R.; Gutman, D. *J. Phys. Chem.* **1983**, *87*, 1812.

(15) Barone, S. B.; Turnipseed, A. A.; Gierczak, T.; Ravishankara, A. R. *J. Phys. Chem.* **1994**, *98*, 11969.

(16) Lee, Y. R.; Chiu, C. L.; Lin, S. M. *J. Chem. Phys.* **1994**, *100*, 7376.

(17) Dominé, F.; Murrells, T. P.; Howard, C. J. *J. Phys. Chem.* **1990**, *94*, 5839.

(18) Tyndall, G. S.; Ravishankara, A. R. *J. Phys. Chem.* **1989**, *93*, 2426.

(19) Turnipseed, A. A.; Barone, S. B.; Ravishankara, A. R. *J. Phys. Chem.* **1993**, *97*, 5926.

(20) Balla, R. J.; Nelson, H. H.; McDonald, J. R. *Chem. Phys* **1986**, *109*, 101.

(21) Atkinson, R.; Baulch, D. L.; Cox, R. A.; Hampson, R. F., Jr.; Kerr, J. A.; Rossi, M. J.; Troe, J. *J. Phys. Chem. Ref. Data* **1997**, *26*, 1329.

(22) Biggs, P.; Canosa-Mas, C. E.; Fracheboud, J.-M.; Parr, A. D.; Shallcross, D. E.; Wayne, R. P.; Caralp, F. *J. Chem. Soc., Faraday Trans.* **1993**, *89*, 4163.

(23) Frost, M. J.; Smith, I. W. M. *J. Chem. Soc., Faraday Trans.* **1990**, *86*, 1751.

(24) Frost, M. J.; Smith, I. W. M. *J. Chem. Soc., Faraday Trans.* **1993**, *89*, 4251.

(25) Yamada, F.; Slagle, I. R.; Gutman, D. *Chem. Phys. Lett.* **1981**, *83*, 409.

(26) Glaenzer, K.; Troe, J. *Ber. Bunsen-Ges. Phys. Chem.* **1974**, *78*, 182.

(27) Dzvonik, M.; Yang, S.; Bersohn, R. *J. Chem. Phys.* **1974**, *61*, 4408.

(28) Gilles, M. K.; Turnipseed, A. A.; Talukdar, R. K.; Rudich, Y.; Villalta, P. W.; Huey, L. G.; Burkholder, J. B.; Ravishankara, A. R. *J. Phys. Chem.* **1996**, *100*, 14005.

(29) Troe, J. *J. Phys. Chem.* **1979**, *83*, 114.

(30) McCaulley, J. A.; Moyle, A. M.; Golde, M. F.; Anderson, S. M.; Kaufman, F. *J. Chem. Soc., Faraday Trans.* **1990**, *86*, 4001.

(31) Rattigan, O. V.; Shallcross, D. E.; Cox, R. A. *J. Chem. Soc., Faraday Trans.*, **1997**, *93*, 2839.

(32) Hearn, C. H.; Turcu, E.; Joens, J. A. *Atmos. Environ.* **1990**, *24A*, 1939.

(33) DeMore, W. B.; Sander, S. P.; Golden, D. M.; Hampson, R. F.; Kurylo, M. J.; Howard, C. J.; Ravishankara, A. R.; Colb, C. E.; Molina, M. J. *JPL Publication 97-4*; Jet Propulsion Laboratory, California Institute of Technology: Pasadena, CA, 1997.

(34) Frisch, M. J.; Trucks, G. W.; Schlegel, H. B.; Gill, P. M. W.; Johnson, B. G.; Robb, M. A.; Cheeseman, J. R.; Keith, T.; Petersson, G. A.; Montgomery, J. A.; Raghavachari, K.; Al-Laham, M. A.; Zakrzewski, V. G.; Ortiz, J. V.; Foresman, J. B.; Cioslowski, J.; Stefanov, B. B.; Nanayakkara, A.; Challacombe, M.; Peng, C. Y.; Ayala, P. Y.; Chen, W.; Wong, M. W.; Andres, J. L.; Replogle, E. S.; Gomperts, R.; Martin, R. L.; Fox, D. J.; Binkley, J. S.; Defrees, D. J.; Baker, J.; Stewart, J. P.; Head-Gordon, M.; Gonzalez, C.; Pople, J. A. *Gaussian 94*, revision E.2; Gaussian, Inc.: Pittsburgh, PA, 1995.

(35) Scott, A. P.; Radom, L. *J. Phys. Chem.* **1996**, *100*, 16502.

(36) Curtiss, L. A.; Raghavachari, K.; Pople, J. A. *J. Chem. Phys.* **1995**, *103*, 4192.

(37) Davis, S. R. *Chem. Phys* **1993**, *97*, 7535.

(38) Frank, A. J.; Turecek, F. *J. Phys. Chem. A* **1999**, *103*, 5348.

(39) Gilbert, R. G.; Smith, S. C.; Jordan, M. J. T. *UNIMOL program suite* (calculation of falloff curves for unimolecular and recombination reactions); School of Chemistry, Sydney University, NSW 2006, Australia, 1993.

(40) Gilbert, R. G.; Smith, S. C. *Theory of Unimolecular and Recombination Reactions*; Blackwell Scientific Publications: Oxford, 1990.

(41) Astholz, D. C.; Troe, J.; Wieters, W. *Chem. Phys* **1979**, *70*, 5107.

(42) Orlando, J. J.; Tyndall, G. S.; Bilde, M.; Ferronato, C.; Wallington, T. J.; Vereecken, L.; Peeters, J. *J. Phys. Chem. A* **1998**, *102*, 8116.

(43) Mellouki, A.; Jourdain, J. L.; Le Bras, G. *Chem. Phys. Lett.* **1988**, *148*, 231.